

Analyst

Accepted Manuscript

This article can be cited before page numbers have been issued, to do this please use: S. Daxini, C. Prüfert, P. A. Reid, P. Bezerra Barros, C. Escobedo, J. Gomez-Cruz, J. A. Barnes and H. Loock, *Analyst*, 2026, DOI: 10.1039/D5AN01181G.



This is an Accepted Manuscript, which has been through the Royal Society of Chemistry peer review process and has been accepted for publication.

Accepted Manuscripts are published online shortly after acceptance, before technical editing, formatting and proof reading. Using this free service, authors can make their results available to the community, in citable form, before we publish the edited article. We will replace this Accepted Manuscript with the edited and formatted Advance Article as soon as it is available.

You can find more information about Accepted Manuscripts in the [Information for Authors](#).

Please note that technical editing may introduce minor changes to the text and/or graphics, which may alter content. The journal's standard [Terms & Conditions](#) and the [Ethical guidelines](#) still apply. In no event shall the Royal Society of Chemistry be held responsible for any errors or omissions in this Accepted Manuscript or any consequences arising from the use of any information it contains.

ARTICLE

Diffusion kinetics of volatile organic compounds monitored by nanohole surface plasmonics

Swapnil Daxini,^a Chris Prüfert,^b Paul Reid,^a Pedro Barros,^c Juan M. Gomez-Cruz,^d Carlos Escobedo,^e Jack A. Barnes,^f and Hans-Peter Look^{*g}

Received 00th January 20xx,
Accepted 00th January 20xx

DOI: 10.1039/x0xx00000x

The extraordinary optical transmission, EOT, through a gold-film nanohole array was used to measure refractive index changes of a thin film of polydimethylsiloxane, PDMS, upon absorption of o-xylene gas. As o-xylene diffuses into the 10 µm thick PDMS film, the film swells slightly and its refractive index increases. The PDMS index change produces a red-shift of the EOT maximum which is observable in a simple optical transmission spectrum. Since the experiments are fast (<200 ms) and precise (<2 × 10⁻⁴ RIU) we can follow the kinetics of the diffusion process with enough accuracy to distinguish two distinct diffusion mechanisms that occur at different time scales.

Introduction

The detection of anthropogenic and biogenic volatile organic compounds (VOCs) is an important field in gas phase analysis and is relevant to, for example, food production, environmental monitoring, health care and industrial processes²⁻⁸. Benzene, toluene, ethylbenzene and xylenes (BTEX) form a subcategory of VOCs, whose monitoring is of particular importance as they pose a considerable risk to human health at high concentration and/or prolonged exposure. Health risks include but are not limited to respiratory diseases, reproductive adversities, and cancer^{9, 10}.

BTEX compounds are typically analysed using separation techniques such as gas chromatography-mass spectrometry (GC-MS), high-performance liquid chromatography (HPLC), and capillary electrophoresis (CE). Samples can be controllably enriched in BTEX concentrations using Solid-Phase Micro-Extraction (SPME), a rapid, solvent-free sample preparation method pioneered by the Pawliszyn group and others^{11, 12}. Polydimethylsiloxane (PDMS) is a commonly used extraction matrix for SPME, as it is an elastic, chemically inert hydrophobic polymer that strongly interacts with non-polar molecules and readily absorbs BTEX from both liquids and gas samples¹³. To optimize PDMS-SPME probes for optimum extraction time and film thickness, it is important to understand the diffusion kinetics of these compounds through PDMS.

The diffusion kinetics through polymers have previously been investigated through gravimetric sensors^{14, 15}, time-lag permeation¹⁶, and through the measurement of refractive index and swelling using a interferometric refractometer^{1, 17}. In this paper, we present a real-time, on-line, continuous, cost-effective VOC sensing method that is based on the phenomenon of extraordinary optical transmission (EOT) to investigate the diffusion kinetics of o-xylene into PDMS.

When light is incident on an array of sub-wavelength holes in a gold or silver film, one observes higher than expected transmission for a range of wavelengths. White light from a broad band light source is thereby filtered such that some colours are blocked, and others are transmitted through the holes to an extent that is higher than expected from classical aperture theory alone¹⁸.

The EOT resonance occurs due to the photonic excitation of surface plasmon polaritons (SPPs) on the metallic surface of the noble metal film. Like surface plasmon resonance (SPR) sensors, EOT-based sensors are sensitive to the changes of the refractive index (RI) at the interface between the metal film and the dielectric medium surrounding it¹⁸⁻²¹. They can be used to measure the refractive index of liquids²² and polymers covering the array²³. Contrary to other optical techniques that are used for VOC detection, nanohole array sensors can be interrogated in transmission mode, allowing for easier alignment, miniaturization and multiplexing^{24, 25}. A conventional absorption spectrometer suffices for the measurement of the EOT signal. The fabrication of the device presented in this work is facile, rapid, and does not require a cleanroom.

Following the publication of the seminal work on EOT by Ebbesen *et al.* in 1998,¹⁸ there have been numerous sensing systems based on nanohole arrays for refractometry^{20, 22, 26}, biosensing^{20, 27, 28}, as well as in multiplexed systems^{28, 29}. Recent work has demonstrated the use of nanohole arrays for gas detection^{30, 31}, though the systems were based on monitoring intensity changes, rather than the

^a Dept. of Physics, University of Victoria, Victoria, B.C., Canada V8N 5C2
^b Inst. of Chemistry, Physical Chemistry, University of Potsdam, 14469 Potsdam, Germany
^c Dept. of Biochemistry, University of Victoria, Victoria, B.C., Canada V8N 5C2
^d Spectra Plasmonics, Kingston, ON, Canada K7L 0E9
^e Dept. of Chemical Engineering, Queen's University, Kingston, ON, Canada K7L 3N6
^f Dept. of Chemistry, Queen's University, Kingston, ON, Canada K7L 3N6
^g Dept. of Chemistry, University of Victoria, Victoria, B.C., Canada V8N 5C2
^{*} hplook@uvic.ca

plasmonic shift induced by refractive index changes, and may therefore be more prone to noise from the light source and detector. The design parameters guiding the optimization of EOT-based sensors were recently reviewed by Asif and Sahin.³²

In the present study, we demonstrate the use of a PDMS-covered EOT system as a novel VOC sensing method. With the high time-resolution and high sensitivity that this sensor affords, we obtain insights into the diffusion kinetics of o-xylene into PDMS. The kinetics of o-xylene diffusion through a thin layer of PDMS are investigated by measuring the peak-shift of the plasmonic signal. To the best of our knowledge, this study is the first application of EOT spectroscopy to the measurement of gaseous analytes, representing, also, the first integration of solid-phase microextraction of gases with EOT-based plasmonic sensing.

In contrast to conventional plasmonic devices, and many previously reported EOT-based sensors, the present configuration eliminates the need for micro- or nanofabrication. The nanohole array is instead obtained by sputter-coating a commercial TEM-support grid with a thin gold film, providing a facile and reproducible platform for optical measurements. The measurement is obtained through a transmission spectrum using a simple optical setup. The system also incorporates a compact and intuitively designed nebulizer that offers high accuracy and adjustability over a wide range of partial pressures. The diffusion model described in the Supplementary Material is derived from a new and rigorous integration of Fick's one-dimensional diffusion law. A comprehensive discussion of this theoretical framework is forthcoming.

Experimental Setup

The PDMS-coated nanohole array (NHA), was mounted into a 3D-printed chamber, and was interrogated in a transmission configuration with collimated light from a broadband light source (LS-1 Tungsten halogen lamp, Ocean Optics, USA). The EOT output spectrum was collected with a fiber-coupled UV-Vis spectrometer (USB4000, Ocean Optics, USA) (Figure 1).

The 3D-printed chamber allows for the introduction of gas either above the PDMS layer or from the underside of the NHA. A nebulizer system was developed to generate different VOC loads in the carrier gas in a compact, resource-efficient way, allowing for adjustable and small loadings (< 4000 ppm) of VOC

in nitrogen gas. The dual gas-stream system can supply the chamber with only carrier gas (N₂) or with analyte-containing gas from the output of the nebulizer system.

The nebulizer consists of two co-axially mounted capillaries, with the inner capillary supplying the liquid VOC through a syringe pump. Due to the steep pressure gradient, strong shear forces are exerted on the liquid at the tip of capillary. This leads to the dispersion of the ejected liquid into a fine mist, i.e. the liquid is nebulized. The flow of heated nitrogen gas from the surrounding larger capillary carries the mist towards the sample chamber while ensuring complete evaporation of the VOC. Since the liquid and gas flow rates can be tightly controlled, the VOC partial pressure of the sample gas can be finely adjusted with about 10 ppm accuracy in the range of 10 ppm to 4000 ppm. A Computational Fluid Dynamics, CFD, simulation of the nebulizer is provided in the Supplementary Information.

Nanohole array fabrication and assembly

The plasmonic NHA sensor head was prepared from a commercial sample-mounting grid designed for transmission electron microscopy, TEM, that we coated with gold. The hexagonal Si₃N₄ nanohole grid (Ted Pella Inc., USA) was plasma-cleaned for 60 s and sputter coated, first, with 5 nm of Cr as an adhesion layer and then, with 100 nm of gold. A scanning electron micrograph, SEM, is provided in the supplementary material (see also Figure 1).

The depth range of the refractive index measurements is governed by the penetration depth of the surface plasmons; thus, it is essential to have strong adhesion between the PDMS and gold layer. As gold bonds only weakly to PDMS, we used (3-mercaptopropyl) trimethoxysilane (MPTMS) (Sigma-Aldrich, USA) as a molecular adhesive³³. The gold-coated NHAs were plasma-cleaned and submersed in a 10 mM ethanolic solution of MPTMS for 20 hours to produce an MPTMS monolayer. The MPTMS was then activated via plasma cleaning for 60 s before a PDMS (Dow Corning Sylgard 184, 10:1 mixing ratio) layer was spin-coated onto the NHA directly thereafter. The NHA was mounted into the spin-coater, the PDMS was drop-cast onto the NHA, and spin-coated with the desired thickness - here 10 μ m. The spin-coating procedure was facilitated by mounting the NHA onto a 3D-printed mount. The 3D-printed component was affixed onto the spin coater with adhesive tape. The thickness was set according to a calibration curve obtained using an optical profiler (see Supplementary Information). After spin-coating, the PDMS film was cured for 10 min at 100°C and 20 min at 70°C on a hotplate. Since the diffusion rate of VOCs through PDMS depends strongly on the crosslinking density of the polymer film, care was taken to maintain a similar PDMS mixing ratio and preparation procedure to reproduce the crosslinking density accurately.

The chamber holding the PDMS-coated NHA was designed in-house and resin-printed using a 3D printer. It consists of three main parts, i.e. two outer plates and one central disc with a slot that holds the NHA. The chamber was designed so that the gas exchange rate in the chamber (≈ 15 ms) is much smaller than the diffusion time constant ($\tau > 10$ s), such that the PDMS diffusion governs the measurements' response time. The plates have a 5 mm x 5 mm square open hole that is turned into an optical window using coverslip squares (Fisher

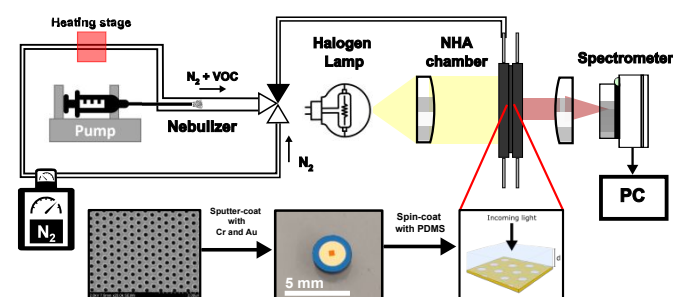


Figure 1 Schematic overview of the setup with the NHA preparation, nebulization stage and optical setup.

Scientific, USA) that are attached and sealed using epoxy resin. On its inside face, each plate has a square center recess that forms the sample chamber. The sample chamber accepts sample gas through a bore connected with 22 needle gauge tubing to the aerosol generator, while the second bore directs the sample gas to waste after it has flown across the PDMS film which faces the white light source. The right part of the chamber (**Figure 1**) has a similar design and, therefore, also permits gas flow across the silicon nitride grid that forms the support for the NHA assembly.

In the present study, all the results were obtained with the sample gas flowing through the PDMS layer towards the gold-coated NHA substrate layer as this gives better insight on the diffusion kinetics through the PDMS layer.

When reversing the gas flow from the NHA substrate towards the unsupported PDMS film surface, we observed a much faster sensor response as the analyte interacts with the plasmonic field immediately. Unfortunately, the measurements were difficult to reproduce, likely because of partial delamination of the PDMS layer due to pressure from the gas flow.

Data pre-processing

The centroid wavelength of the EOT peak was used as a measure of the wavelength of the EOT resonance instead of the maximum of the peak. The centroid corresponds to the “centre of mass” and was calculated using the top 50% of the EOT transmission peak. Using the centroid wavelength is advantageous, if the EOT contribution of interest (here arising from plasmonic interactions at the PDMS-Au interface) spectrally overlaps with other EOT contributions such as those from the substrate-Au interface. Prior to determining the peak centroid, the Savitzky-Golay filter was used on the spectrum to reduce the noise, resulting in fewer outliers in the centroid calculation.

We averaged ten consecutive EOT spectra, and the average centroid wavelength is calculated with its respective standard error and with acquisition rates ranging from 200 ms to 2s.

Theoretical models

Mole fraction calculations

After calibration of the sensor one can determine the refractive index of the PDMS from the experimentally observed using centroid wavelength of the EOT spectrum. Next, the average mole fraction, $\bar{X}(t)$, of the analyte that is absorbed in the section of the film interrogated by the surface plasmon polaritons can be calculated from the film's refractive index, n_{mix} , using (1), an equation that had been derived previously¹,

$$\bar{X}(t) = \frac{P_{\text{PDMS}} \left[1 - \left(\frac{n_{\text{PDMS}}^2 + 2}{n_{\text{PDMS}}^2 - 1} \right) \left(\frac{n_{\text{mix}}^2(t) - 1}{n_{\text{mix}}^2(t) + 2} \right) \right]}{P_{\text{PDMS}} \left[1 - \left(\frac{n_{\text{PDMS}}^2 + 2}{n_{\text{PDMS}}^2 - 1} \right) \left(\frac{n_{\text{mix}}^2(t) - 1}{n_{\text{mix}}^2(t) + 2} \right) \left(1 + \frac{\Delta d(t)}{d_0} \right) \right] - P_{\text{Analyte}}} \quad (1)$$

In deriving (1), it is assumed that the Lorenz-Lorentz equation holds, i.e. that molar polarizabilities, P_i , are linearly additive. Note that refractive indices, n_i , are not linearly additive. In this

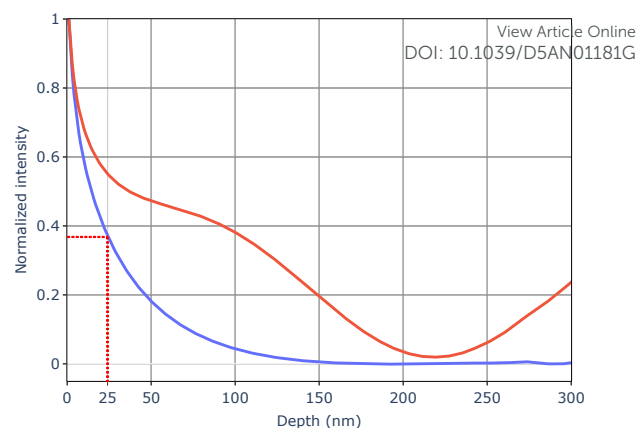


Figure 2 Calculation of the depth of the evanescent wave into the PDMS layer. The red curve shows the total average electric field intensity as a function of distance from the NHA support, which includes the contribution from the reflected field. After subtracting the sinusoidal contribution from the reflected radiation, the exponential curve (blue) shows an evanescent intensity decay length of 25 nm, i.e. the length at which the intensity decays by $1/e$.

case, we also assume that swelling of the film is negligible ($\Delta d = 0$). Although it has been observed that PDMS swells by up to 50% after 72 hours of exposure to a saturated xylene atmosphere³⁴, the assumption holds in our experiments, since the sorption experiments were much shorter and at a lower xylene concentration. Indeed, the maximum swelling was measured to be between 2-5% and assumed negligible for the modelling. The maximum swelling upon absorption was determined from a weak thin film interference spectrum observed in many of the EOT spectra (see Supplementary Information).

Diffusion constants of the VOCs

Since the experiments are conducted at temperatures well above the PDMS glass transition temperature, $T_g = -123^\circ\text{C}$ ³⁵, the analyte migration into a polymer can be modelled by a one-dimensional Fickian diffusion mechanism³⁶

$$\frac{dX}{dt} = D \frac{\partial^2 X}{\partial y^2} \quad (2)$$

The PDMS layer on the surface is thin compared to its lateral extension, and the hole diameter is orders of magnitude smaller than the film thickness. Therefore, the problem was analysed as one-dimensional diffusion through a plane of finite thickness having an infinite reservoir of analyte gas above the polymeric sorption film. Most of this film is supported by the gold film which is assumed to be an impenetrable substrate (described as a “supported film”), and a smaller fraction is suspended above the nanoholes (“free-standing film”).

We now introduce, briefly, the kinetic model of the absorption and desorption of an analyte into a thin film supported by an array of nanoholes. In our derivation we integrate Crank's solutions for a one-dimensional diffusion problem³⁷. When neglecting lateral diffusion, the problem can be understood as a linear combination of Crank's solution for a film mounted on an impermeable support and the solution for a free-standing film.

Equations (6) and (8) for a supported film have been presented, previously¹. Their derivations by integration of the Crank's equations, as well as the derivation of the new equations (5) and (7) for a free-standing film, are given in the Supplementary Information. The average mole fraction of the analyte over the film sliver sampled by the evanescent wave near metal-film interface is given by \bar{X}_{SF} for a supported film (SF), and by \bar{X}_{FSF} for a free-standing film (FSF). The slivers thickness is determined by the FDTD simulation, see **Figure 2**. The weighted linear combination of these contributions is determined separately for absorption processes (*abs*) in equations (5) and (6) and desorption processes (*des*) in equations (7) and (8). In these equations X_{∞} is the equilibrium mole fraction in the film, and the diffusion coefficient D is calculated from the fit to (3).

The film thickness, $d = 10.2 \mu\text{m}$ was obtained using an optical profiler (see Supplementary Information), and δy is the effective amplitude of the evanescent plasmonic wave into the PDMS and is obtained by modelling - see below and **Figure 2**. The weighing coefficients can be estimated using the cross-sectional areas of holes (FSF) and the gold film (SF). The total sensing area is $2.0 \times 10^5 \mu\text{m}^2$, and the nanoholes, representing the FSM, account for $4.0 \times 10^4 \mu\text{m}^2$ or 20% of the total area. Therefore, the linear combination representing the total solvent mole fraction can be estimated as:

$$\begin{aligned}\bar{X}_{abs} &= 0.8\bar{X}_{abs,SF} + 0.2\bar{X}_{abs,FSF} \\ \bar{X}_{des} &= 0.8\bar{X}_{des,SF} + 0.2\bar{X}_{des,FSF}\end{aligned}\quad (3)$$

A more rigorous determination of this 4:1 ratio, accounting for the overlap of the evanescent wave with the PDMS film, is given below and in the Supplementary Information.

As will be discussed below, most processes are best analysed as concurrent sorption processes having *two* different diffusion rates given by D_1 and D_2 , and (3) is therefore best written as

$$\begin{aligned}\bar{X}_{abs} &= 0.8[a_1\bar{X}_{abs,SF}(D_1) + a_2\bar{X}_{abs,SF}(D_2)] \\ &\quad + 0.2[a_1\bar{X}_{abs,FSF}(D_1) + a_2\bar{X}_{abs,FSF}(D_2)] \\ \bar{X}_{des} &= 0.8[b_1\bar{X}_{des,SF}(D_1) + b_2\bar{X}_{des,SF}(D_2)] \\ &\quad + 0.2[b_1\bar{X}_{des,FSF}(D_1) + b_2\bar{X}_{des,FSF}(D_2)]\end{aligned}\quad (4)$$

where a_1, a_2, b_1, b_2, D_1 and D_2 are the parameters that are optimized in a least-squares fitting algorithm.

EOT simulation

To investigate the spatial extent, δy , of surface plasmon resonance (SPR) interactions within the system we conducted a three-dimensional finite-difference time-domain (FDTD) simulation (Tidy3D 2.8.4, Flexcompute). Periodic boundary conditions were applied along the x and y directions ($1.4 \mu\text{m}$ and $1.2 \mu\text{m}$, respectively), corresponding to a small section of

$$\bar{X}_j(t)_{abs,FSF} = a_j \left[\frac{\delta y}{2d} + \frac{2d}{\pi^2 \delta y} \sum_{i=1}^{\infty} \frac{(-1)^i}{i^2} \exp\left(-\frac{D_j(t-t_0)i^2\pi^2}{d^2}\right) \left(1 - \cos\frac{i\pi\delta y}{d}\right) \right]; j = 1, 2 \quad (5)$$

$$\bar{X}_j(t)_{abs,SF} = a_j \left[1 - \frac{8d}{\pi^2 \delta y} \sum_{i=0}^{\infty} \frac{(-1)^i}{(2i+1)^2} \exp\left(-\frac{D_j(t-t_0)(2i+1)^2\pi^2}{4d^2}\right) \sin\left(\frac{(2i+1)\pi\delta y}{2d}\right) \right] \quad (6)$$

$$\bar{X}_j(t)_{des,FSF} = b_j \left[\frac{4d}{\delta y \pi^2} \sum_{i=0}^{\infty} \frac{1}{(2i+1)^2} \exp\left(-\frac{D_j(t-t_0)(2i+1)^2\pi^2}{d^2}\right) \left(1 - \cos\frac{(2i+1)\pi\delta y}{d}\right) \right]; j = 1, 2 \quad (7)$$

$$\bar{X}_j(t)_{des,SF} = b_j \left[\frac{8d}{\pi^2 \delta y} \sum_{i=0}^{\infty} \frac{(-1)^i}{(2i+1)^2} \exp\left(-\frac{D_j(t-t_0)(2i+1)^2\pi^2}{4d^2}\right) \sin\left(\frac{(2i+1)\pi\delta y}{2d}\right) \right] \quad (8)$$

the hexagonal NHA. Along the z -axis, perfectly matched layers, PMLs, were implemented to absorb outgoing waves and reduce reflections. To ensure the highest resolution near the plane of interaction an override mesh (size: 7 nm in x - and y -direction and 0.5 nm in z -direction) was employed throughout the segment and with a height of 600 nm, centred about the TEM grid. The PDMS film, the Cr adhesion layer, and the silicon nitride substrate were modelled using the Sellmeier dispersion relation with parameters obtained from the Tidy3D database³⁸⁻⁴⁰, while the optical response of gold was described using a Drude model, as it more accurately captures its plasmonic behaviour⁴¹.

The FDTD simulation was used to determine the electric fields' spatial distribution across the gold surface and at various depths within the PDMS. This was used to estimate the ratio of the sensing areas between the supported film and the free-standing film in (3). Details in the Supplementary Information show that the ratio is nearly identical to the 4:1 ratio estimated from the fractional areas in the previous section.

In addition, the integrated field intensity at the SPR resonance wavelengths was used to evaluate the decay lengths of the SPR-induced fields into the PDMS material to estimate $\delta y = 25 \text{ nm}$, as the effective decay length of the evanescent plasmonic wave (**Figure 2**). In this figure, the normalized average electric field intensity is calculated in 0.5 nm steps into the PDMS layer. The sinusoidal reflected field was subtracted from the average intensity to retrieve the evanescent field from the plasmonic interaction at the interface. This decay length, δy , governs the thickness of the layer in which the refractive index change can be measured, i.e. it corresponds to the bounds of the integrals that lead to equations (5)-(8) (Supplementary Information).

The wavelengths of the EOT resonances for a periodic hexagonal lattice array of nanoholes can also be approximated using momentum conservation matching conditions⁴², given by

$$\lambda_{\max,i,j} = \frac{\Lambda}{\sqrt{\frac{4}{3}(i^2 + ij + j^2)}} \sqrt{\frac{\epsilon_m \epsilon_d}{\epsilon_m + \epsilon_d}} \quad (9)$$

where Λ is the period of array, i and j are resonance orders, ϵ_m and ϵ_d are the dielectric constants of the metal and dielectric, respectively. **Figure 3** shows experimental EOT spectra for two different refractive indices. The location of approximate

resonances due to the PDMS-Au interface and Au-Si₃N₄ interface are predicted by Eq. (9) and plotted as gold and gray arrows respectively.

Calibration curve and sensitivity

The diffusion mechanism of o-xylene through PDMS can be determined by measuring the time-dependent mole fractions of o-xylene in the PDMS layer adjacent to the gold-film. The mole fractions are obtained from the refractive indices during that process. Over the small refractive index range that we study, the experimentally obtained wavelength shift of the EOT maximum (obtained using the centroid of the top 50% of the peak) correlates linearly with the change in the refractive index of the dielectric medium above the gold layer. A calibration series of mixtures of glycerol (C₃H₈O₃, $n = 1.475$) and water ($n = 1.333$ at 589 nm) was used to obtain the sensor's sensitivity as $S = 170 \pm 3$ nm per refractive index unit (RIU) (Figure 4). The refractive indices of the water-glycerol mixtures were

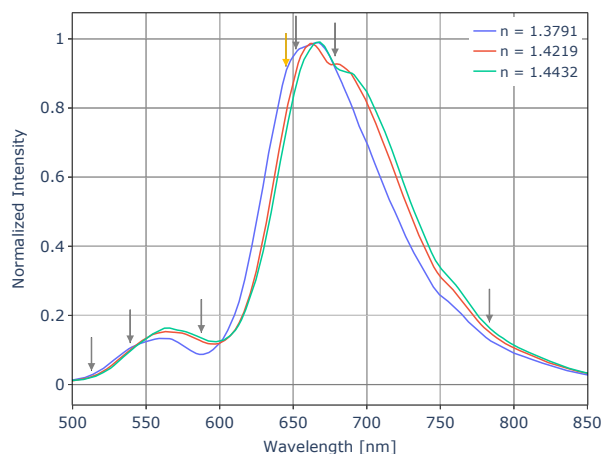


Figure 3 EOT resonance spectrum for solutions with different refractive indices flowing over the NHA. The arrows represent the wavelength of the resonances due to plasmonic interaction as predicted by Eq. (9) for the Au-Si₃N₄ (gray) and dielectric-Au (gold) interfaces. As the refractive index of the solution above the Au changes, we observe a changing peak shape as the contribution of the dielectric-Au EOT resonance shifts.

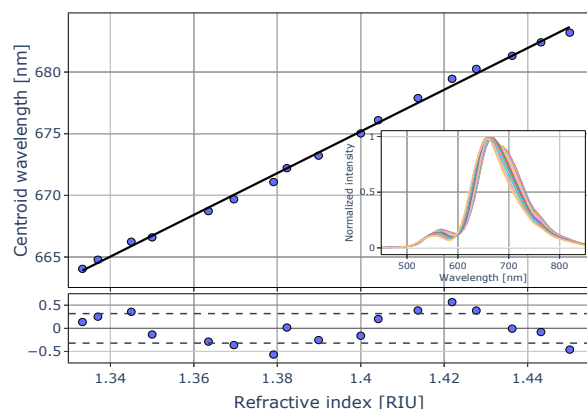


Figure 4 Calibration of the sensor using mixtures of glycerol and water. The spectra of all solutions are shown in the inset. The linear fit yields the sensitivity of the RI measurement as $S = 170 \pm 3$ nm/RIU. The width of the 1 σ -confidence interval (0.8 nm) indicates that refractive index can be measured with an uncertainty of $\Delta n = 0.002$ RIU.

determined using a handheld digital refractometer (Item #81150-56, Cole-Parmer). The confidence intervals and the residuals indicate that the refractive index in this range can be obtained with an average 1 σ uncertainty of $\Delta n = 0.002$ RIU, which is limited by the accuracy of the reference refractometer. To perform the calibration, the NHA was placed in a PDMS mould having a 50 μ m open channel to allow for the flow of calibration solutions using a peristaltic pump. Each solution was directed over the NHA for a minimum of 60s and the average centroid wavelength for each mixture was obtained.

Results

Figure 5 shows the mole fraction of o-xylene in the boundary layer to the gold surface, measured through the observed shift of the centroid wavelength, as a function of time and at different o-xylene partial pressures (30 Pa = 295 ppm = 1 μ L/min). By inspection, it is apparent that with increasing gas concentrations the rate of uptake of o-xylene into the film increases, and that the desorption rate also increases. In addition, the equilibrium value that is reached for each of the o-xylene partial pressures increases with increasing concentration, consistent with SPME principles¹². It is also apparent that gas concentrations above 1770 ppm (179 Pa; 6 μ L/min) show evidence for a second uptake process that occurs at a slower rate and leads to a much higher loading of the film. Especially the desorption curves show that the second slower process is time-delayed, as there is a clear step in the desorption curves.

In order to quantify the diffusion constants of the diffusion of o-xylene into PDMS, the absorption and desorption curves were fitted separately to (5)-(8). The curves were fit (LMfit python package⁴³) with two diffusion coefficients i.e. using a weighted sum of the respective curves (5)-(8) as expressed in (4). **Figure 6** shows an example of the least-squares fit of the absorption and desorption using 2360 ppm o-xylene (238 Pa, 8 μ L/min flow

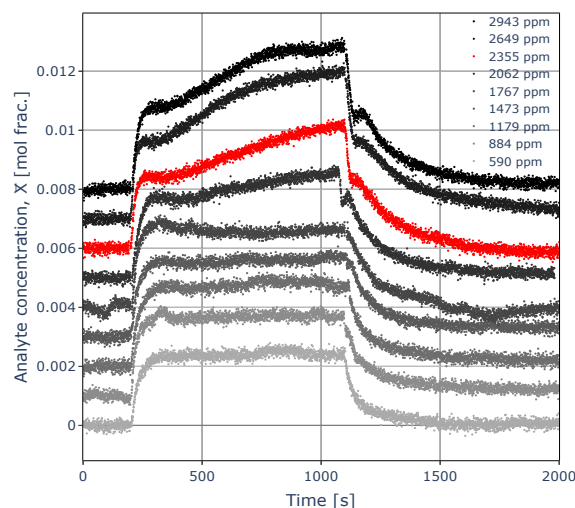


Figure 5 Absorption and desorption curves for a nitrogen gas flow of 750 mL/min loaded with different concentrations of o-xylene sent through the nebulizer (with an added offset for visualization). For the first 200 s, pure N₂ is flown over the chamber to establish a baseline, followed by 900 s of o-xylene/N₂ flow and pure N₂ flow again for absorption and desorption respectively. The data highlighted in red are also shown in Fig 6.

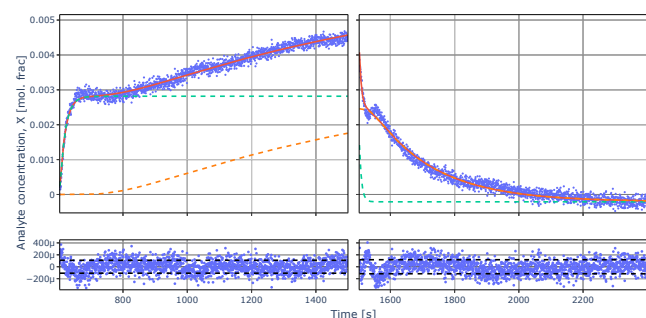


Figure 6 Fitting of sorption curves with diffusion equations (4). The fit (solid red line) is a linear combination of the bi-exponential fit (dashed green and orange line) for the absorption ($D_1 = 3.0 \times 10^{-8} \text{ cm}^2/\text{s}$, $D_2 = 9.0 \times 10^{-10} \text{ cm}^2/\text{s}$) and desorption ($D_1 = 3.5 \times 10^{-8} \text{ cm}^2/\text{s}$, $D_2 = 1.9 \times 10^{-10} \text{ cm}^2/\text{s}$). The residuals are displayed below each graph.

rate) to equation (4) having two different rates. Here, the fast and slow sorption processes were assumed to start at the same time and to occur concurrently. We note that the step in **Figure 6**, and, indeed, in all sorption curves with concentrations higher than 1770 ppm indicates that concurrent absorption may *not* be a good model. Introducing the time delay of the slower process as an additional fitting constant gave diffusion rates that were similar but had a larger uncertainty, since the additional fitting parameter made the model less constrained. For these practical reasons we retained the assumption that the slow and fast processes start at the same time in our analysis.

An analysis similar to that shown in **Figure 6** was conducted for all concentrations of o-xylene and the two average diffusion coefficients for each flow rate were obtained by fitting. Each datum in **Figure 7** represents the average fitted diffusion coefficients, D_1 , D_2 , of at least three runs, with the uncertainty derived from standard error. The size of the circular data markers is proportional to the asymptotic concentration, a_1 , a_2 , b_1 , b_2 , of the respective equation in (4).

The diffusion constants for the absorption processes are averaged to $D_1 = (22 \pm 6) \times 10^{-9} \text{ cm}^2\text{s}^{-1}$ and $D_2 = (0.9 \pm 1.5) \times 10^{-9} \text{ cm}^2\text{s}^{-1}$, whereas averaging the diffusion constants for the desorption processes yields $D_1 = (29 \pm 21) \times 10^{-9} \text{ cm}^2\text{s}^{-1}$ and $D_2 = (2.5 \pm 0.7) \times 10^{-9} \text{ cm}^2\text{s}^{-1}$ (see Supplementary information for the data table **Figure 7**). These values are in fair agreement with those given by Saunders *et al.*¹ for the absorption of m-xylene into PDMS $D_1 = (30 \pm 10) \times 10^{-9} \text{ cm}^2\text{s}^{-1}$ and $D_2 = (4 \pm 3) \times 10^{-9} \text{ cm}^2\text{s}^{-1}$ and for the respective desorption processes $D_1 = (60 \pm 20) \times 10^{-9} \text{ cm}^2\text{s}^{-1}$ and $D_2 = (5 \pm 5) \times 10^{-9} \text{ cm}^2\text{s}^{-1}$.

Discussion

The residuals in **Figure 6** may be used to estimate the uncertainty of the measurement. We can express this uncertainty either as the mole fraction of o-xylene in the film, $\delta X = \pm 0.0001$, or as the precision of the refractive index measurement $\delta n_{\text{mix}} = \pm 0.0001$ (see eq. (1)). The precision of the refractive index measurement is much better than the accuracy, $\pm \Delta n = 0.002$, obtained through the calibration curve in **Figure 4**, which also depends on the accuracy of the RI values determined for the calibration solutions.

Figure 7 shows that even at low concentrations of o-xylene the absorption and desorption curves can be well-fit using a process

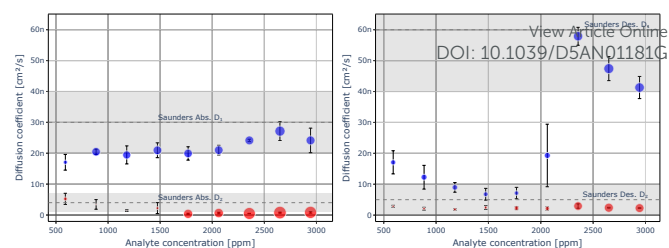


Figure 7 Average absorption (left) and desorption (right) diffusion coefficients (D_1 and D_2 given in cm^2/s) with the dashed grey line and shaded region representing previously obtained diffusion coefficients¹ for m-xylene with their uncertainties. The desorption D_1 diffusion coefficient for 2062 ppm (7 $\mu\text{L}/\text{min}$) shows a large uncertainty as not all fits were successful in capturing the second desorption process. A data table is provided in the supplementary information.

having two distinct diffusion constants. A data table is given in the Supplementary Information. Both diffusion constants are consistent with earlier measurements of diffusion of m-xylene (not o-xylene) into a 20 μm -thick PDMS film interrogated by glancing angle thin-film interferometry.¹ The 1σ uncertainties of these previously obtained diffusion constants are given as grey bands in **Figure 7**.

The more robust measurements at concentrations > 1770 ppm (6 $\mu\text{L}/\text{min}$) give diffusion constants that fall into the lower range of previously obtained values. The difference may be due to the different diffusion rates of m-xylene used previously and o-xylene used here, the slightly different composition and crosslinking densities inherent with commercial PDMS formulations, or due to different boundary layer chemistry – our PDMS film is chemically bonded to a gold film, whereas in the previous measurement PDMS was spin-cast onto glass¹, a plexiglass plate⁴⁴ or a rubber membrane⁴⁵.

Importantly, the observed diffusion kinetics provide further evidence for a two-stage diffusion process as first reported by Saunders *et al.*¹ In their model, the VOC fills the pores within the PDMS resulting in a rapid change in refractive index. This process is followed by a slower absorption that changes the internal structure of the PDMS and causes it to swell. Both processes become faster with increasing VOC concentration of the surrounding gas, i.e. they are consistent with a first-order process.

The diffusion coefficients we obtained are consistent with measurements by Saunders *et al.* but they were 10-fold lower than those reported by other methods^{14, 44–46} for o-xylene and its isomers. This discrepancy has been rationalized by Saunders *et al.* as being due to 1) the difference in PDMS manufacturers which has been shown to result in different degrees of crosslinking, thereby altering the diffusion kinetics through the polymer, and 2) the inconsistency of the mathematical modelling of the diffusion process through the PDMS, which can change the diffusion constant by a factor of 2 for different models as reported by Lue *et al.*^{14, 15}.

The second point is worth emphasizing: to the best of our knowledge, equations (6) and (8) describing the diffusion through a supported film and our new equations (5) and (7) for a free-standing film have not been used widely before. They arise from exact integration of Crank's equations³⁷ and are derived from the one-dimensional diffusion case described by

Fick's second law (2). The more commonly used kinetic laws are usually written for the absorption process as

$$\bar{X}'(t)_{abs} = X'_{\infty} \left[1 - \exp\left(-\frac{D'(t-t_0)}{d^2}\right) \right] \quad (10)$$

and for the desorption as

$$\bar{X}'(t)_{des} = X'_{\infty} \exp\left(-\frac{D'(t-t_0)}{d^2}\right). \quad (11)$$

with little regard on whether the film is supported or not. Equations (10) and (11) are first-order approximations to exact diffusion equations (5) to (8), and yield diffusion constants that may be quite different compared to the exact equations.

In a forthcoming publication we will discuss the diffusion models for a supported film and for a free-standing film in more detail.

Conclusion

A simple and comparably inexpensive device exploiting the extraordinary optical transmission through a gold-covered nanohole array was used to record refractive index changes with an accuracy of 0.002 RIU and is likely limited by our ability to determine the refractive index of the calibration solutions. The precision of the measurement (0.0001 RIU) is much higher and can be obtained from the wavelength change associated with the uptake of a high index VOC gas into a PDMS film that was applied as an SPME layer to the surface of the gold-NHA. The precision is ultimately limited by intensity noise in the spectrum which affects to a small extent the precision of the centroid wavelength determination. The temporal resolution of 200 ms/measurement is limited by the combination of the spectral acquisition rate and the time it takes to determine the centroid wavelength, which is the only parameter we retain from the measurements.

These uptake and desorption measurements allowed us to determine accurate diffusion constants using equations that were obtained by an integration of Crank's equations, which in turn are exact representations of Fick's second diffusion law. The measurements are consistent with previously reported values that were obtained on a similar chemical system but with a different device. The accuracy of the diffusion constants, D , is limited by the accuracy with which we know the film thickness, d , since any fit can only obtain the rise time as a ratio of d^2 and D , as apparent in the diffusion time constant

$$\tau = \frac{4d^2}{D\pi^2} \quad (12)$$

Consider that for $d = (10 \pm 2) \mu\text{m}$ and an assumed $D = 10 \times 10^{-9} \text{ cm}^2/\text{s}$, the uncertainty in the reported absolute diffusion constant would be 40%.

Finally, we submit that the presented device can be seen as a single receptor in an "electronic nose", which may be combined with other receptors using different polymer extraction

matrices to obtain an estimate of the chemical composition of a gas sample.

DOI: 10.1039/D5AN01181G

Declarations

Authors' contribution

SD has contributed to conceptualization, investigation, data collection and analysis, visualization and to all stages of the writing process. CP has contributed to conceptualization, investigation, data curation, writing, review, and editing. PR performed many of the optical simulations. PB performed many of the adsorption and desorption measurements. JGC helped set up the experiments and advised on the chemical model. JAB derived the diffusion model equations. CE and HPL contributed to conceptualization, funding acquisition, project administration, supervision, writing, and editing.

Competing interests

The authors declare no competing interests.

Funding

This research was financially supported by the Natural Sciences and Engineering Research council of Canada through the Discovery Grants program awarded to CE and HPL. The authors also acknowledge financial contributions of the University of Victoria and Queen's University.

References

1. J. E. Saunders, H. Chen, C. Brauer, M. Clayton and H. P. Loock, *Soft Matter*, 2018, **14**, 2206-2218.
2. P. Ciccio, C. Silibello, S. Finardi, N. Pepe, P. Ciccio, F. Rapparini, L. Neri, S. Fares, F. Brilli, M. Mircea, E. Magliulo and R. Baraldi, *Agricultural and Forest Meteorology*, 2023, **328**, 19, 109255.
3. R. Epping and M. Koch, *Molecules*, 2023, **28**, 19, 1598.
4. C. Di Fiore, P. Pandolfi, F. Carriera, A. Iannone, G. Settimo, V. Mattei and P. Avino, *Appl. Sci.-Basel*, 2023, **13**, 11, 7344.
5. X. Bai, W. Liu, B. Wu, S. Liu, X. Liu, Y. Hao, W. Liang, S. Lin, L. Luo, S. Zhao, C. Zhu, J. Hao and H. Tian, *Environmental Pollution*, 2023, **316**, 120600.
6. M. Fan, T. F. Rakotondrabe, G. Chen and M. Guo, *Food Chemistry*, 2023, **418**, 135950.
7. A. Erler, D. Riebe, T. Beitz, H. G. Löhmansröben, D. Grothshetkamp, T. Kunz and F. J. Methner, *Journal of Mass Spectrometry*, 2020, **55**, 10, e4501.
8. Q. Pan, Q.-Y. Liu, J. Zheng, Y.-H. Li, S. Xiang, X.-J. Sun and X.-S. He, *Environment International*, 2023, **174**, 107886.
9. R. Montero-Montoya, R. López-Vargas and O. Arellano-Aguilar, *Annals of Global Health*, 2018, **84**, 225-238.
10. M. Masekameni, R. Moolla, M. Gulumian and D. Brouwer, *International Journal of Environmental Research and Public Health*, 2018, **16**, 95.
11. C. L. Arthur and J. Pawliszyn, *Analytical Chemistry*, 1990, **62**, 2145-2148.
12. J. Pawliszyn, *Applications of solid phase microextraction*, Royal Society of Chemistry, Cambridge, 1st edition edn., 1999.
13. S. Seethapathy and T. Górecki, *Analytica Chimica Acta*, 2012, **750**, 48-62.
14. S. J. Lue, S. F. Wang, L. D. Wang, W. W. Chen, K.-M. Du and S. Y. Wu, *Desalination*, 2008, **233**, 277-285.
15. G. Dakroub, T. Duguet, C. Lacaze-Dufaure, S. Roualdes, A. van der Lee, D. Rebiscoul and V. Rouessac, *Plasma*, 2023, **6**, 563-576.
16. S. Sato, M. Suzuki, S. Kanehashi and K. Nagai, *Journal of Membrane Science*, 2010, **360**, 352-362.



17. J. E. Saunders, H. Chen, C. Brauer, M. Clayton, W. Chen, J. A. Barnes and H. P. Looock, *Soft Matter*, 2015, **11**, 8746-8757.
18. T. W. Ebbesen, H. J. Lezec, H. F. Ghaemi, T. Thio and P. A. Wolff, *Nature*, 1998, **391**, 667-669.
19. S. Nair, J. Gomez-Cruz, Á. Manjarrez-Hernandez, G. Ascanio, R. G. Sabat and C. Escobedo, *Analyst*, 2020, **145**, 2133-2142.
20. J. Gomez-Cruz, S. Nair, A. Manjarrez-Hernandez, S. Gavilanes-Parra, G. Ascanio and C. Escobedo, *Biosens. Bioelectron.*, 2018, **106**, 105-110.
21. S. G. Rodrigo, F. de Leon-Perez and L. Martin-Moreno, *Proceedings of the IEEE*, 2016, **104**, 2288-2306.
22. X. Lan, B. Cheng, Q. Yang, J. Huang, H. Wang, Y. Ma, H. Shi and H. Xiao, *Sensors and Actuators B: Chemical*, 2014, **193**, 95-99.
23. A. G. Brolo, S. C. Kwok, M. G. Moffitt, R. Gordon, J. Riordon and K. L. Kavanagh, *Journal of the American Chemical Society*, 2005, **127**, 14936-14941.
24. C. Escobedo, *Lab on a Chip*, 2013, **13**, 2445-2463.
25. J. Ferreira, M. J. L. Santos, M. M. Rahman, A. G. Brolo, R. Gordon, D. Sinton and E. M. Girotto, *Journal of the American Chemical Society*, 2008, **131**, 436-437.
26. J. Gomez-Cruz, S. Nair, G. Ascanio and C. Escobedo, SPIE Optics + Photonics Conference on Plasmonics - Design, Materials, Fabrication, Characterization, and Applications XV, San Diego, CA, 2017, SPIE-Int Soc Optical Engineering, 10346,
27. R. Gordon, D. Sinton, K. L. Kavanagh and A. G. Brolo, *Accounts of Chemical Research*, 2008, **41**, 1049-1057.
28. J. C. Yang, J. Ji, J. M. Hogle and D. N. Larson, *Biosens. Bioelectron.*, 2009, **24**, 2334-2338.
29. J. Ji, J. G. O'Connell, D. J. Carter and D. N. Larson, *Analytical Chemistry*, 2008, **80**, 2491-2498.
30. L. Kalvoda, J. Jakoubková, M. Burda, P. Kwiecien, I. Richter and J. Kopecek, *Sensors*, 2023, **23**, 10, 4065.
31. Y. Zhao, K. Mukherjee, K. D. Benkstein, L. Sun, K. L. Steffens, C. B. Montgomery, S. Guo, S. Semancik and M. E. Zaghoul, *Nanoscale*, 2019, **11**, 11922-11932.
32. H. Asif and R. Sahin, *Applied Physics B-Lasers and Optics*, 2025, **131**, 37.
33. A. González-López, J. Gomez-Cruz, G. Ascanio and C. Escobedo, *IEEE Sensors Journal*, 2025, **25**, 23685-23691.
34. C. V. Rumens, M. A. Ziai, K. E. Belsey, J. C. Batchelor and S. J. Holder, *Journal of Materials Chemistry C*, 2015, **3**, 10091-10098.
35. P. V. Lambeck, *Measurement Science and Technology*, 2006, **17**, R93-R116.
36. X.-D. Wang and O. S. Wolfbeis, *Analytical Chemistry*, 2016, **88**, 203-227.
37. J. Crank, *The Mathematics of Diffusion*, Oxford University Press, New York, 2nd Edition edn., 2011.
38. R. Niemeier and J. D. Rogers, *Appl. Opt.*, 2019, **58**, 6152-6156.
39. K. Luke, Y. Okawachi, M. R. E. Lamont, A. L. Gaeta and M. Lipson, *Opt. Lett.*, 2015, **40**, 4823-4826.
40. M. N. Polyanskiy, *Scientific Data*, 2024, **11**, 19, 94.
41. A. D. Rakić, A. B. Djurišić, J. M. Elazar and M. L. Majewski, *Appl. Opt.*, 1998, **37**, 5271-5283.
42. T. Thio, H. F. Ghaemi, H. J. Lezec, P. A. Wolff and T. W. Ebbesen, *J. Opt. Soc. Am. B*, 1999, **16**, 1743-1748.
43. M. Newville, R. Otten, A. Nelson, T. Stensitzki, A. Ingargiola, D. Allan, A. Fox, F. Carter and M. Rawlik, *LMFIT: Non-Linear Least-Squares Minimization and Curve-Fitting for Python*, Zenodo, bibcode: 2016ascl.soft06014N, 2016.
44. Y.-M. Sun and J. Chen, *Journal of Applied Polymer Science*, 1994, **51**, 1797-1804.
45. K.-S. Oh, Y.-M. Koo and K.-W. Jung, *International Journal of Mass Spectrometry*, 2006, **253**, 65-70. DOI: 10.1039/D5AN01181G
46. E. Boscaini, M. L. Alexander, P. Prazeller and T. D. Märk, *International Journal of Mass Spectrometry*, 2004, **239**, 179-186.

ARTICLE

Data Availability: Diffusion kinetics of volatile organic compounds monitored by nanohole surface plasmonics

Received 00th January 20xx,
Accepted 00th January 20xx

DOI: 10.1039/x0xx00000x

Swapnil Daxini,^a Chris Prüfert,^b Paul Reid,^a Pedro Barros,^c Juan M. Gomez-Cruz,^d Carlos Escobedo,^e Jack A. Barnes,^f and Hans-Peter Look^{*g}

The data sets used to generate the diffusion constants are available on **Borealis**, the Canadian Dataverse Repository, a bilingual, multi-disciplinary, secure, Canadian research data repository, supported by academic libraries and research institutions across Canada. Borealis supports discovery, management, sharing, and preservation of Canadian research data. The data and the code (functions described in equations (3)-(6)) can be obtained from Daxini, Swapnil, 2025, "Replication Data for: Diffusion kinetics of volatile organic compounds monitored by nanohole surface plasmonics", <https://doi.org/10.5683/SP3/EAVGPF>, Borealis, DRAFT VERSION, UNF:6:FzR6blogj0hvt4lpoQEuTg== [fileUNF]

(Note to reviewers: digital object identifiers will be active at the proof stage)

